Preliminary retrieval of solar wind latitude distribution from Solar Wind Anisotropies/SOHO observations

E Kyrölä, T Summanen, W Schmidt, T Mäkinen, Eric Quémerais, Jean-Loup Bertaux, Rosine Lallement, Jorge Costa

JOURNAL OF GEOPHYSICAL RESEARCH, VOL. 103, NO. A7, PAGES 14,523–14,538, JULY 1, 1998

Preliminary retrieval of solar wind latitude distribution from Solar Wind Anisotropies/SOHO observations

E. Kyrölä, T. Summanen, W. Schmidt, and T. Mäkinen

Geophysical Research Division, Finnish Meteorological Institute, Helsinki, Finland

E. Quemerais, J.-L. Bertaux, R. Lallement, and J. Costa

Service d'Aeronomie du Centre National de la Recherce Scientifique, Verrieres le Buisson, France

Abstract. The Solar Wind Anisotropies (SWAN) instrument on board the SOHO spacecraft measures Lyman alpha radiation emanating mainly from neutral hydrogen gas in the solar neighborhood. This gas is part of the local interstellar cloud in which the Sun and the heliosphere are immersed. Measurements of Lyman alpha can be used to infer the local cloud characteristics like the velocity and the direction of the flow, gas temperature, and density. The strong interaction between the Sun and the neutral hydrogen gas also makes possible investigations of solar characteristics by Lyman alpha measurements. In this work we will concentrate on deriving the latitudinal distribution of solar-induced ionization from SWAN Lyman alpha maps measured in 1996 at a time of the solar minimum. From the ionization we derive the distribution of the solar wind mass flux. SWAN Lyman alpha data show that the ionization and the mass flux are nearly flat for all solar latitudes except the narrow belt from -20° to 20° around the solar equator. In this region, ionization and the solar wind mass flux show a definite increase, which can be seen as an intensity depression in the Lyman alpha data from directions near the ecliptic. These results confirm earlier in situ measurements by Ulysses during the present minimum and Lyman alpha measurements by Prognoz satellites 20 years ago.

1. Introduction

The diffuse Lyman alpha radiation, which can be detected all over the heliosphere, reveals the presence of neutral hydrogen in the heliosphere. This hydrogen is now understood to have an origin outside the heliosphere; it is a relatively small (about 1 parsec) interstellar cloud surrounding the Sun [see, e.g., *Lallement and Bertin* 1992]. The Sun and the cloud, often called the local cloud, are moving with a velocity of about 25 km/s with respect to each other.

If there were no movement, ionization brought by solar UV photons and by the solar wind would carve a large ionization cavity around the Sun. This so-called Strömgren sphere would reach out to 1000 AU. The movement of the cloud diminishes the influence of the Sun on the cloud so that the actual ionization cavity extends only a few tens of AU from the Sun. Therefore a substantial number of neutral hydrogen atoms reach the immediate neighborhood of the Sun where they are in place to scatter solar Lyman alpha photons. This makes it possible for a spacecraft bound to a near-Earth orbit to map neutral hydrogen atoms near the Sun via observing Lyman alpha radiation [*Holzer* 1977; *Bertaux et al.*, 1996b; *Lallement et al.*, 1995; *Summanen*, 1996b].

The knowledge of the neutral hydrogen distribution can be used to estimate the ionizing power exerted by the Sun. Ionization is brought mainly by charge exchange reactions between neutral H atoms and solar wind protons. A smaller part (about 20%) is caused by solar EUV radiation. Solar wind characteristics are quite well known around the ecliptic from several in situ measurements. At other latitudes there has been virtually no data before 1992 because of the difficulties imposed by sending out-of-ecliptic spacecraft. Since 1992 the Ulysses mission has given us the first in situ measurements of the solar wind at high latitudes. Despite this success it is clear that remote sensing measurements of the solar wind, like Lyman alpha, remain to be valuable tools in monitoring the solar wind distribution in a long-term manner.

The investigations of solar wind characteristics by Lyman alpha measurements were started by *Kumar and Broadfoot* [1978, 1979]. They found that by assuming an anisotropic ionization a better agreement between the models and Lyman alpha data was produced. The Lyman alpha group at Service d'Aeronomie in Paris

Paper number 97JA03432.
0148-0227/98/97JA-03432$09.00

published several investigations of the solar wind distribution based on Lyman alpha measurements by Prognoz satellites in 1976-1977 during the solar minimum [*Bertaux and Lallement* 1984; *Bertaux et al.,* 1985, *Lallement et al.,* 1984, 1985a, b]. They found that the Lyman alpha patterns could be reasonably modeled assuming a simple sinusoidal variation of the ionization rate as a function of the solar latitude. Ionisation around the solar equator was estimated to be 40% greater than over the solar poles. Subsequently the solar wind mass flux was predicted to show a similar albeit somewhat smaller anisotropy. The significance of the solar wind mass flux distribution on the solar wind energy balance was investigated as well [*Lallement et al.,* 1986]. Analysis of Lyman alpha data from other satellites gave similar results to Prognoz [*Ajello,* 1990]. Further studies on Prognoz data showed that a better agreement between data and models was achieved using a discrete model for the dependence of the ionization rate on the solar latitude [*Summanen et al.,* 1993, 1994, 1997; *Summanen,* 1996b]. The ensuing ionization showed a fairly flat variation except near the equator where a clear ionization bulge was measured. It is now quite generally accepted that the solar wind is not isotropic (see, however, the ongoing discussion by *Scherer and Fahr* [1995], *Bertaux et al.* [1997a], and *Scherer and Fahr* [1997]).

The solar wind distribution results from Prognoz Lyman alpha observations have been least partly validated by the recent in situ measurements by the Ulysses spacecraft. The mass flux results were astonishingly similar with these two methods even if the underlying measurements were separated by almost 20 years from each other [*Summanen et al.,* 1997; *Goldstein et al.,* 1996]. While this was a great accomplishment it would, of course, be important to get a more complete validation between in situ and the remote sensing Lyman alpha method. The possibility has now materialized when the European Space Agency (ESA)-NASA solar observatory SOHO includes a new Lyman alpha instrument, Solar Wind Anisotropies (SWAN), and Ulysses is continuing its measurements. It is now possible to acquire simultaneous measurements and also follow the progression of the solar cycle in results.

The SWAN instrument is a Lyman alpha instrument capable for a full-sky mapping [*Bertaux et al.,* 1988b, 1995]. This task is a first of its kind. Earlier instruments were only capable to measure a part of the sky, and many were obstructed by Earth's geocoronal Lyman alpha radiation. Since the beginning of 1996 SWAN has measured full sky Lyman alpha maps and also restricted area maps to investigate comets.

In this paper we present a first analysis of the SWAN's principal scientific objective: the solar wind anisotropy. For a more general presentation of SWAN first results, see *Bertaux et al.* [1997b]. The SWAN data we use are selected full-sky maps which have been measured during SWAN's first operational year, 1996. Data are corrected only for clear instrumental effects like flat fields of the detectors. The model we use to interpret the data is based on concepts which are well understood and also computationally efficient in treating quite large data sets. We are using the single-scattering model for Lyman alpha. We assume that H gas far away from the Sun shows a Maxwellian velocity distribution and finally that all parameters are independent of the solar cycle. The modeling aspects which are moving into the standard model but which we discard here are the multiple-scattering model for Lyman alpha photons [*Keller et al.,* 1981; *Quemerais and Bertaux* 1993a; *Scherer and Fahr,* 1996], the modification of the far away distribution of the hydrogen gas by the heliospheric interface [*Ripken and Fahr,* 1983; *Osterbart and Fahr,* 1992; *Baranov and Malama* 1993; *Quemerais et al.,* 1993b; *Fahr,* 1996; *Lallement,* 1996], the solar cycle modulation of the H gas distribution near the Sun [*Kyrölä et al.,* 1994; *Rucinski and Bzowski,* 1995; *Summanen,* 1996a], and a possible anisotropy in the solar UV field [*Pryor et al.,* 1996]. These refinements will be considered in further studies when the characteristics of SWAN data are more completely understood.

2. SWAN Instrument and Data

The SWAN instrument consists of two sensor units which are served by a common electronic unit (for a detailed presentation, see *Bertaux et al.* [1995, 1997b]). The sensor units are mounted on the opposite sides of the SOHO spacecraft. One sensor sees mainly the north ecliptic hemisphere and the other the south ecliptic hemisphere. The SOHO coordinate axes are such that the x-axis is pointing toward the Sun center, and the plane formed by the x and z-axes includes the solar rotation axis. The upper ecliptical sensor is located therefore on the $+z$ side and the lower ecliptical sensor on $-z$ side. As SOHO moves along a halo orbit around the L1 Lagrangian point at about 1.5 10^6 km from the Earth, it is out off the ecliptic but only at most 1° seen from the Sun. This and the tilt of the solar rotation axis mean that each sensor sees also some of the other hemisphere. The SOHO coordinate axis and the location of SWAN sensors are shown in Figure 1.

Each sensor includes a sensor head with two aspherical mirrors. The mirrors are mounted on step motors. By activating these motors a 2π space angle can be scanned in the sky by each sensor. The radiation is focused on a detector through a hydrogen cell which is filled by molecular hydrogen which is transparent to Lyman alpha light. It includes, however, a tungsten filament which can be electronically heated and used to dissociate hydrogen molecules to atoms which in turn interact intensively with incoming radiation. Absorption in the hydrogen cell atoms will burn a spectral hole to the intensity distribution of the incoming radiation. The location of the hole depends on the relative velocity of the cell (i.e. spacecraft) and the source of the radiation through the Doppler shift. The width and the depth of the hole are dependent on the temperature of the gas in the cell and on the cell's optical depth. If either the Doppler shift or the optical depth can be changed, the cell measurements can be considered to yield spectrometric capabilities.

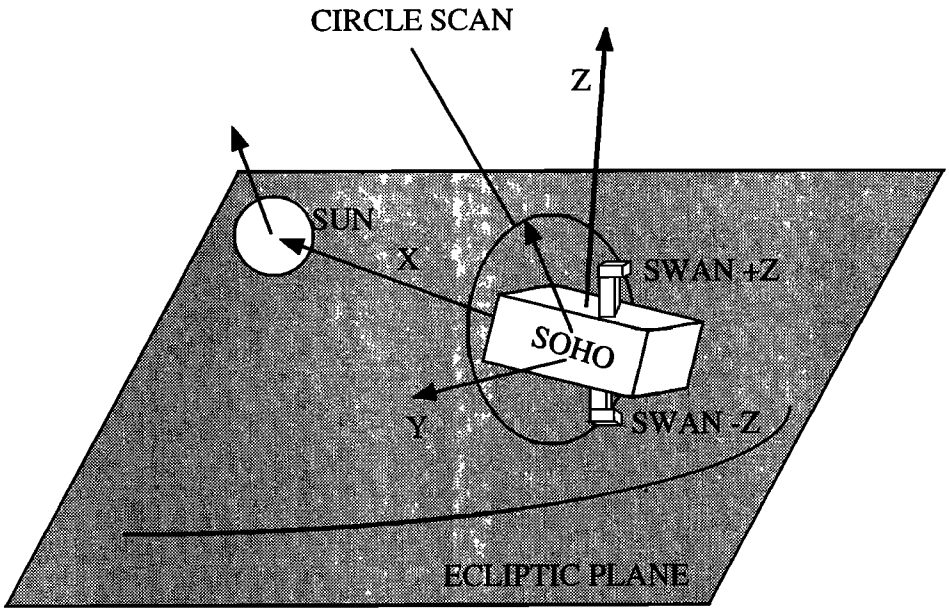

Figure 1. SOHO spacecraft, SOHO coordinate axis, SWAN sensors, and the Sun with the rotation axis. The circle is the path that lines of sight follow in the data sets used in this work.

The SWAN detector is a multichannel plate with 27 pixels. One pixel sees 1°x1° field of view. The spectral band recorded is 1170-1700 Å. One of these pixels is covered by BaF_2, and it is used to filter out Lyman alpha radiation. One pixel is for the dark current monitoring. The integration time can be varied. Most often it is about 13 seconds for any particular line of sight.

Counts from the 25 pixels form the basic set in the data analysis. Besides count values, it is imperative to know the lines of sight of pixels, the location, and the velocity of the spacecraft when measurements were taken. In order to make effective mapping, different pixel sensitivities must be known and corrected in data (so-called flat fielding). Because SWAN includes two sensors, their mutual calibration must also be established. If the H cell is activated, we need to know the cell temperature and its optical depth. In an ideal case we would still like to know the absolute calibration of our instrument.

SWAN has already measured successfully over 2 years, and a representative set of full-sky maps is available. Here we take only one example. Plate 1 shows a full-sky map from March 28, 1996. The location of SOHO is shown in Figure 2. Intensity is in Rayleigh units; that is we have applied absolute calibration. The 4π view of the sky is shown using the so-called sinusoidal projection. This projection gives a correct weighting to the polar regions. The ecliptic plane runs horizontally in the middle of the map. The direction of the Sun, Earth, and SOHO are displayed. The approximate inflow direction of the interstellar wind is also shown.

The most spectacular phenomenon in Plate 1 is the large localized bright spot in the right top corner. It is the Hyakutake comet. It emits water vapor which is dissociated into H atoms. These H atoms form a huge cloud which effectively scatters solar Lyman alpha [*Bertaux et al.*, 1997c]. The interstellar hydrogen cloud is manifested with the color variation especially in the middle plane of Plate 1. The upwind direction pops up for its large intensity, whereas in the downwind, much of the neutral H gas is ionized and consequently intensity is depressed. The bright spots all around the Plate 1 are hot UV stars which are so dominating because of the wide spectral band pass of SWAN. There are so many of these stars that they seriously harm our data reduction particularly near the galactic plane.

3. Data Sets Used for Analysis

We have used the SWAN full-sky maps as a starting point in the data analysis. The data content in a full sky map is, however, so large that a direct comparison to models is presently computationally quite demanding. Therefore we have confined data analysis in this analysis paper to a more restricted data set. We have extracted full-circle scans from full-sky maps. These data sets are similar to the ones obtained from the Prognoz satellites in 1976-1977. Prognoz was a spinning spacecraft, and the Lyman alpha detector measured Lyman alpha radiation during the spinning. Now we do this spinning artificially. The scan is determined as follows. We use the SOHO fixed axis coordinate system (see Figure 1) and accept all data values whose line of sight unit vector ($\vec{s}$) has only a small x-component ($|s_x| \leq 0.01$). This circle set of lines of sight is approximately perpendicular to the SOHO x-axis. Because SOHO is all the time near the ecliptic plane the scan plane is nearly perpendicular to the ecliptic plane and the lines of sight cover all the ecliptical latitudes. A given scan covers, however, only two longitudes, so that several spacecraft locations are needed to get a longitudinal coverage by these data sets.

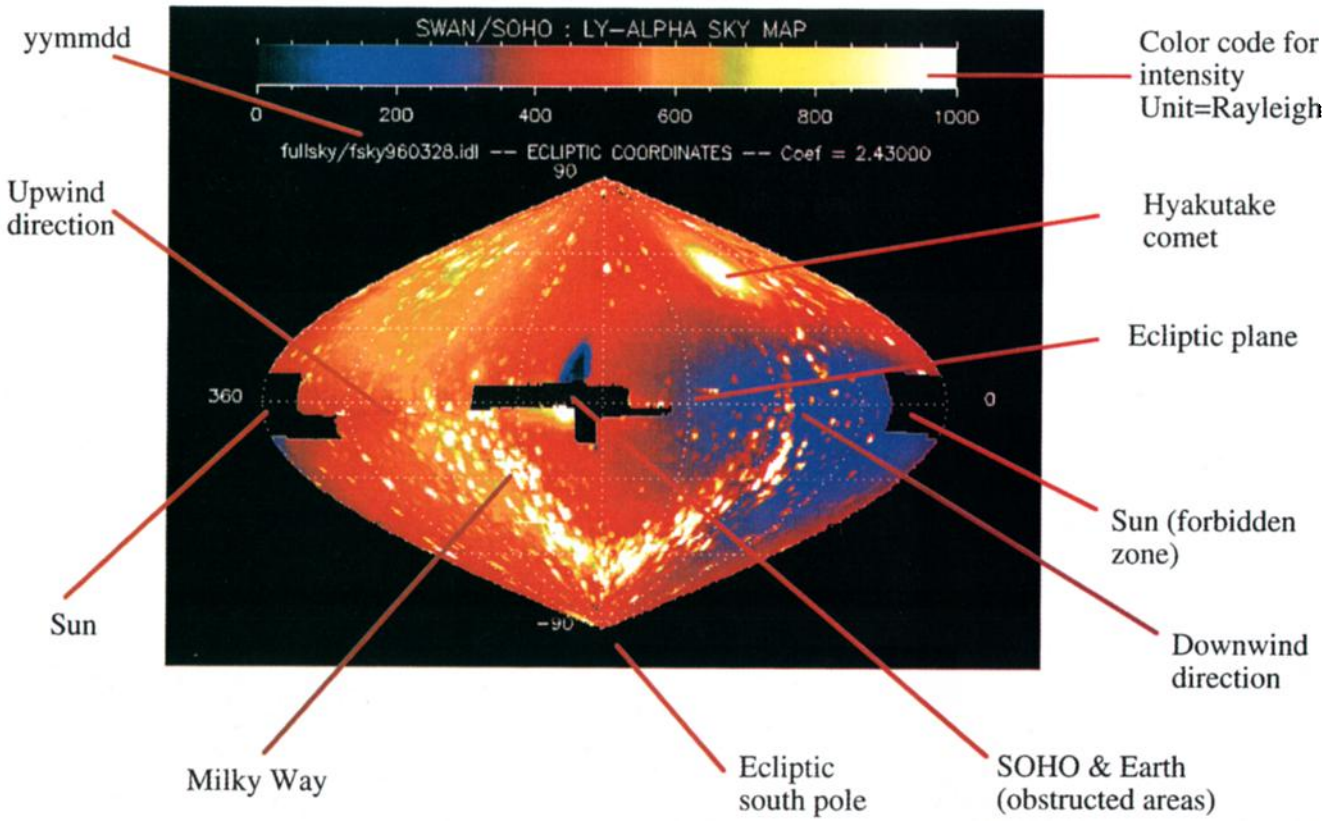

Plate 1. SWAN all sky map March 28, 1996.

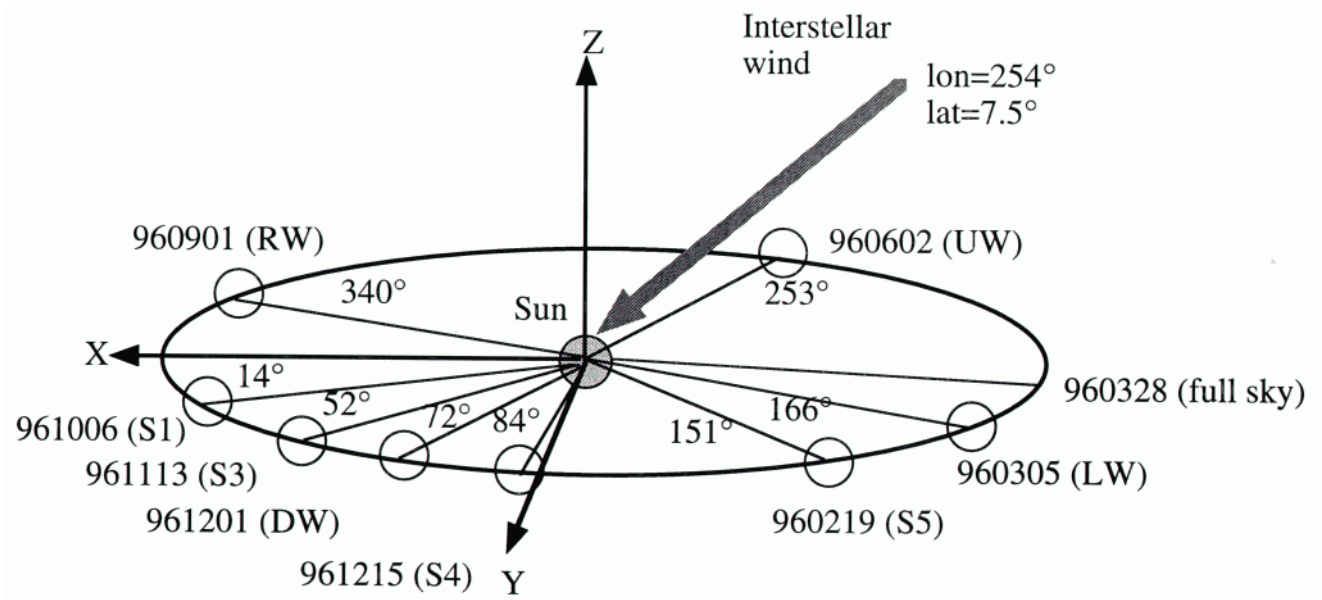

Figure 2. Locations of SOHO for the data sets used in this work are shown. Longitudes and latitudes refer to the ecliptical coordinate system. UW, RW, LW, and DW are upwind, right wind, left wind, and downwind, respectively.

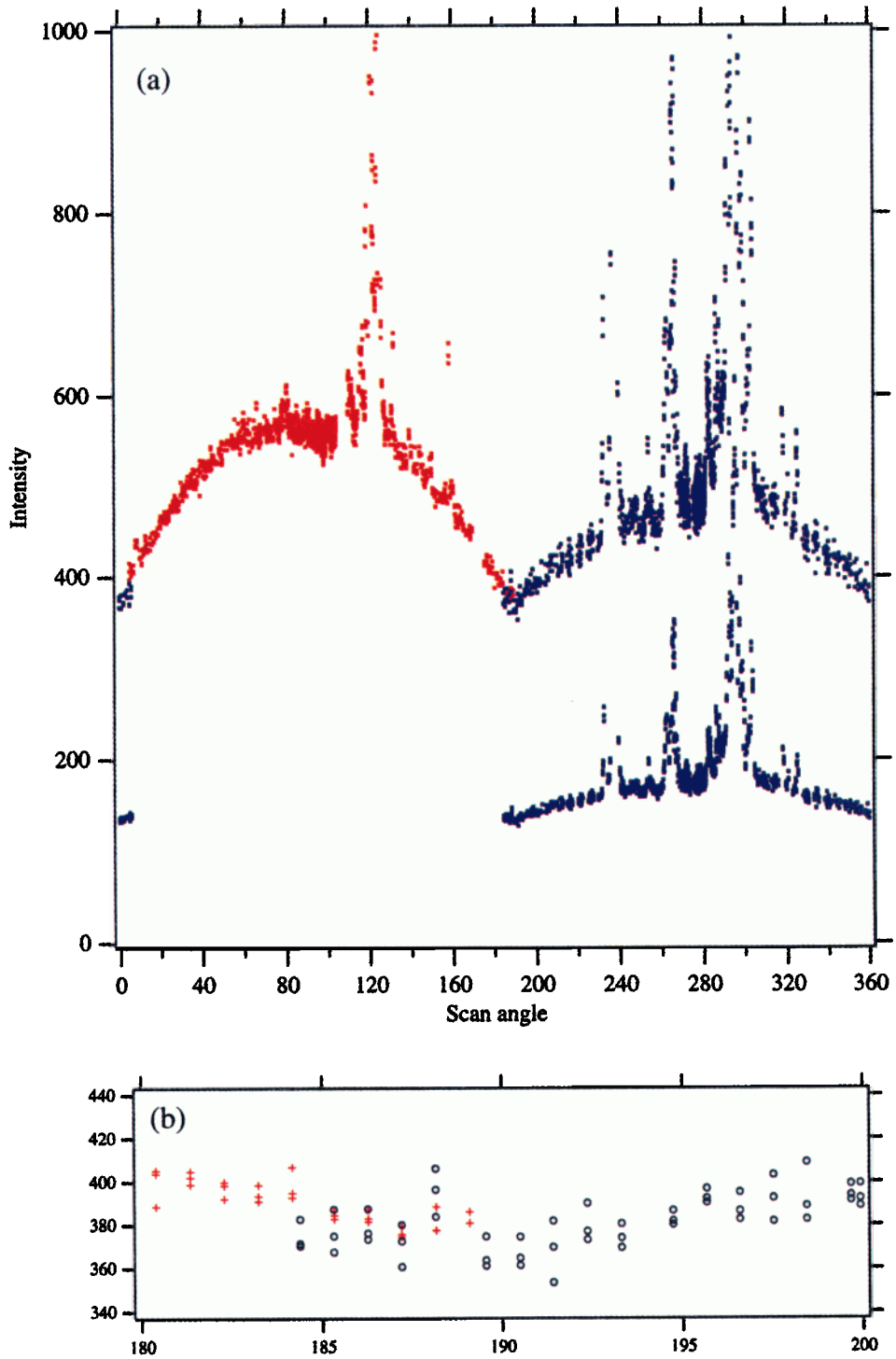

Plate 2. (a) Calibration between the plus and minus sensors. Red points are from the plus sensor and blue points from the minus sensor. Because of the partial overlap of field of view of sensors we can intercalibrate both sensors. (b) The visual matching of results from the plus sensor (crosses) and from the minus sensor (circles) are shown here.

We have selected four different ecliptical longitudes to obtain enough coverage for lines of sight. These four are selected in such a way that we can have lines of sight directed to the interstellar wind approach direction (the so-called upwind direction), to the downwind direction, as well as to the perpendicular directions with respect to the wind. Notice that the assumption of knowing the interstellar wind direction is not important. Its validity can be studied using SWAN data. The four different data set locations are shown in Figure 2.

Plate 2 shows an example of how we obtain the data sets that are compared to models. These particular data are from June 2, 1996. The red curve is obtained from the +Z detector pixels with lines of sight in the slice just defined. The blue curve shows the corresponding points from -Z detector. The efficiency of the -Z detector is much less than of the +Z detector. Fortunately, the plus and minus data sets include some the almost same lines of sight around the ecliptic (in the center and both sides of Plate 2a), and using this fact, we can recalibrate -Z values. Plate 2b shows an enlargement of the ecliptic junction point. Finally we apply the absolute calibration by dividing both sets by a factor 0.84 to convert counts per second into Rayleigh units (this step is not shown in Plate 2). The calibration factor has been determined from a simultaneous measurement with the Hubble Space Telescope (see *Bertaux et al.*, [1997b]).

In Figure 3 we have shown photometric data from a circular scan and the corresponding reduction factor plot. Both data sets show relatively large fluctuations. Some of these are easily seen to be stars and we have done some preliminary identifications based on the Bright Star Catalogue (BSC) (see Figure 3a). The ecliptic latitude and longitude positions from BSC and from the SWAN data differ at most by 1° degree. This can arise in some cases from the fact that a star intensity maximum is not inside the area of the circle scan. In some cases the identification itself is under suspicion. SWAN's line of sight determinations also have some un-

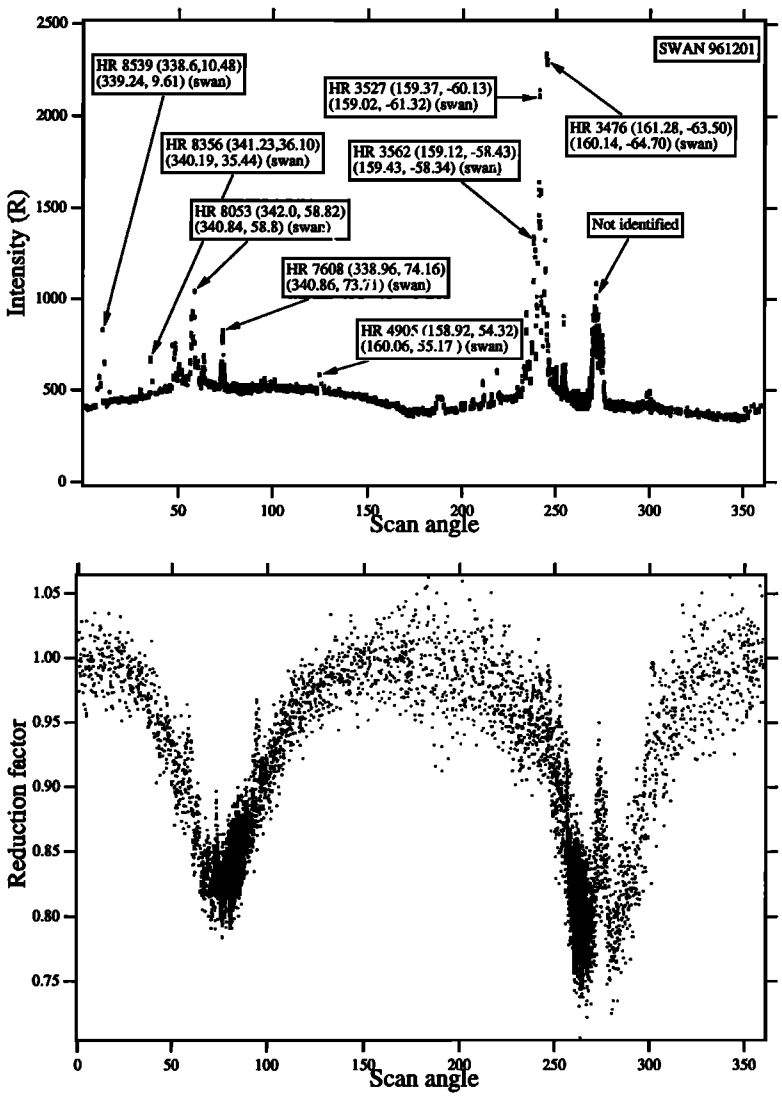

Figure 3. (top) A circular scan with several star identifications. (bottom) In the lower part a corresponding reduction factor plot.

certainty. As the errors are only up to 1°, this will not hurt the anisotropy studies. The occurrence of several stars along the scan is more troublesome. Removing them by any means leaves large data gaps which can, of course, be patched by interpolation but with the obvious increased uncertainty. At this point we do not attempt to remove any stars from data.

Our restriction to Prognoz-type data is because there exist several studies of solar wind anisotropy based on Prognoz data (see the references quoted in the introduction). It is also interesting to compare the Prognoz and SWAN data sets directly with each other. Figures 4a-4d show four different Prognoz data sets for which a corresponding SWAN data set was available. The Prognoz and SWAN data are separated in time by 19 years. We have made the comparison easier by bringing the SWAN and Prognoz data sets approximately to the same intensity level (the scaling factors are mentioned in the figure caption). It is obvious that Prognoz data are much less affected by stars because of a narrow wavelength filter implemented in the Prognoz Lyman alpha instrument. However, there are large data gaps in Prognoz data because of geocoronal contamination. It is clear from Figures 4a-4d that despite the 19 years separation

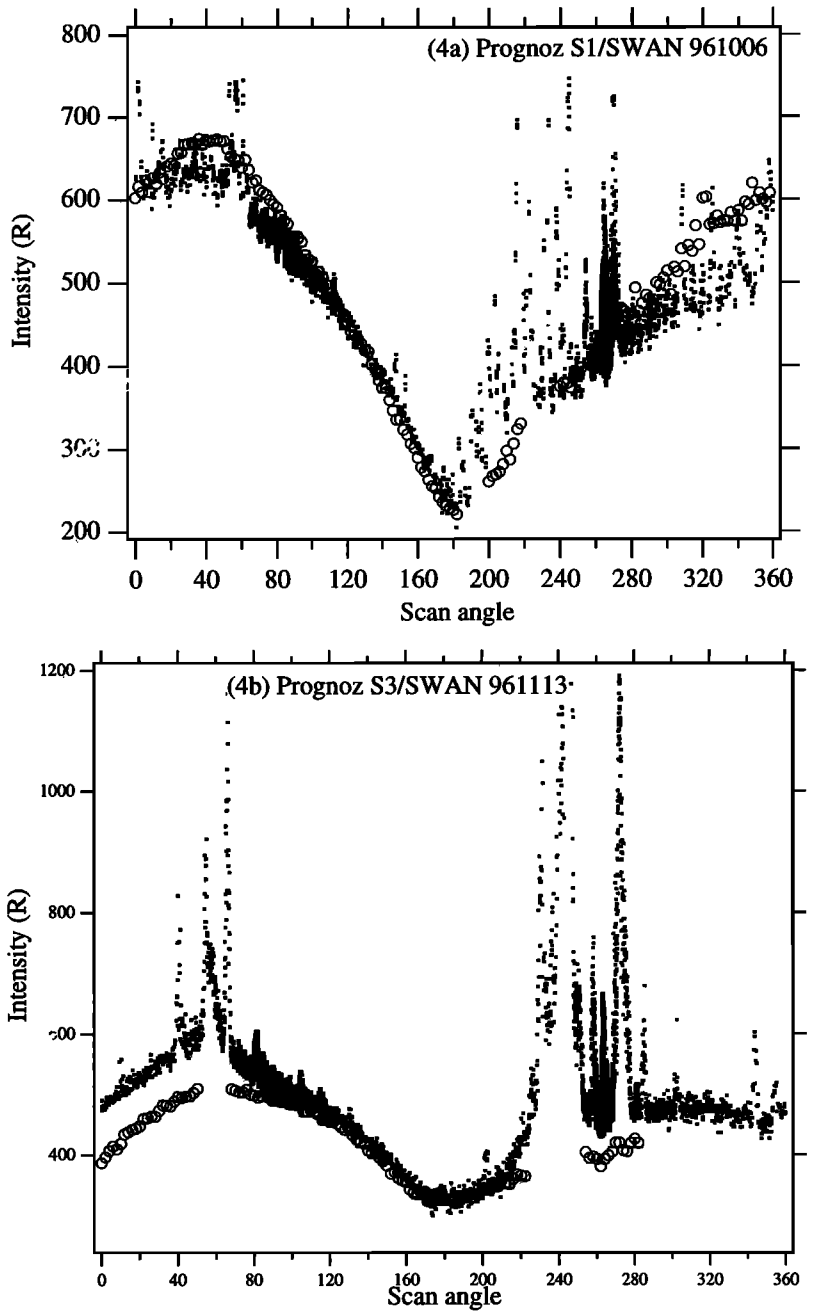

Figure 4. Four different Prognoz measurements (circles) together with the corresponding SWAN scans. Absolute calibration has been applied for SWAN data. In (a) the Prognoz data has been multiplied by a factor 0.62, in (b) by 0.58, in (c) by 0.62, and in (d) by 0.92.

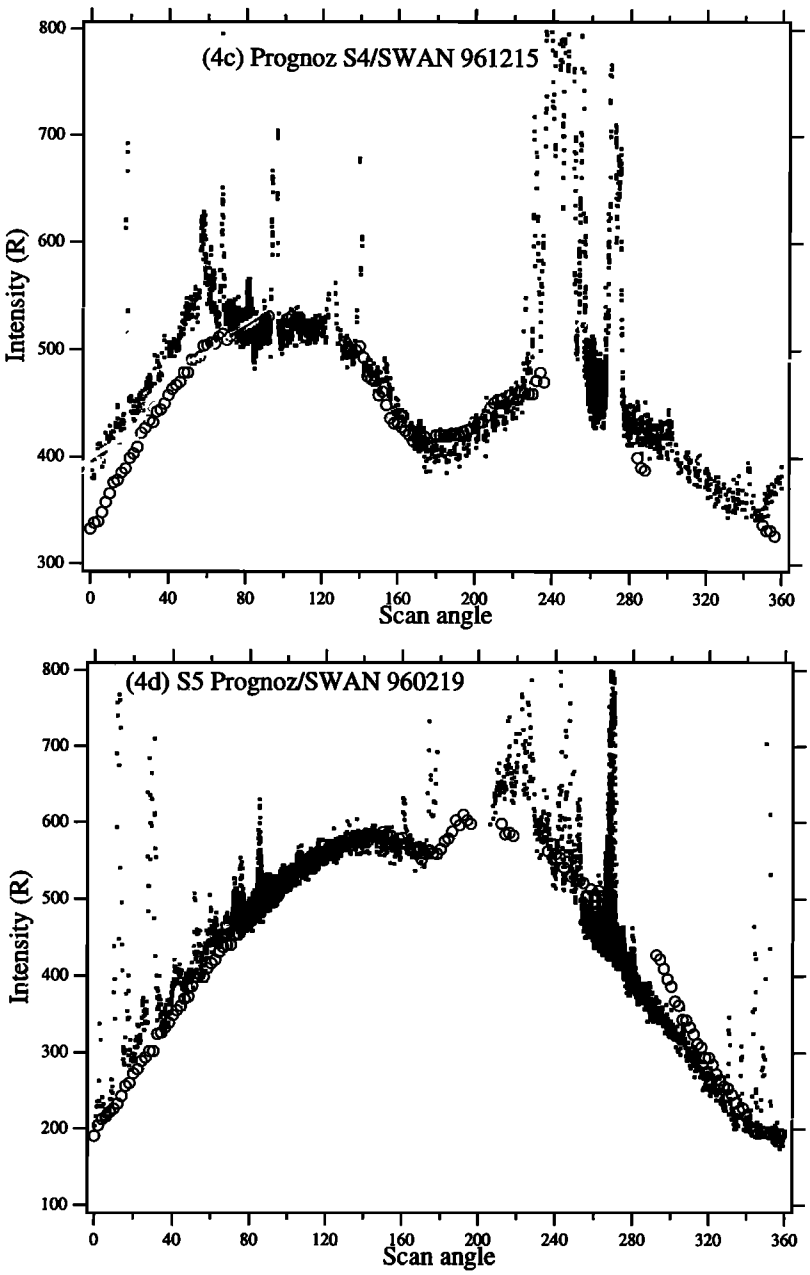

Figure 4. (continued)

the overall shapes are very similar, albeit some changes in levels are discernible.

4. Modeling

Recording the Lyman alpha intensity from different directions means a kind of tomographic mapping of the solar surroundings. SWAN measurements constitute an interior tomography problem; that is, we are looking at the scattering or absorbing medium from inside, whereas in the ordinary tomography we probe the medium under investigation by measurements outside the medium. The tomograhic construction of the scattering hydrogen gas density has been attempted in the SWAN project, but so far it has escaped success. The basic reason is that SOHO is bound to a 1 AU orbit which does not yield enough variation for the lines of sight toward any given space volume further away from the Sun. Therefore, in this work we will trust on the traditional approach to analyze measurements. This comprises modeling the neutral gas distribution (density and velocity distributions) using some reasonable modeling parameters. The modeling is completed by introducing a radiative transfer model to calculate the Lyman alpha intensity. By comparing the modeled intensity with the one measured by SWAN we acquire information on the correctness of our parameter selections. Repeating this kind of comparisons with several parameter selections, we aim at the optimal parameters giving the best agreement with the data. The level of

agreement between the data and the model also reveals how adequate our model is for explaining SWAN data.

There exists two different levels of modeling of the counts observed by SWAN. We can analyze the photometric content of the incoming signal, or we can analyze the spectrometric content of the signal. Calculation of the photometric content of the signal is computationally quite a fast task compared to the spectral simulation. In the SWAN data analysis the spectral simulation is, however, needed when we try to simulate the SWAN signal measured at the time when the H cell is turned on. In that case we are aiming to calculate the so-called reduction factor defined by

$$R(T_{cell}, \tau_{cell}) = \frac{N_{on}}{N_{off}} \tag{1}$$

The arguments T_{cell} and τ_{cell} are the cell temperature and the cell optical depth, respectively. The noteworthy aspect in this quantity is that it is by definition free of photometric calibration factors. Figure 3b, however, showed that the present reduction factor determinations from SWAN data display large fluctuations, some of these are even related to stars. Obviously more work is needed to produce high-quality reduction factor data. Therefore, in this preliminary work we will not employ this data in analysis.

In order to simulate the SWAN counts by the photometric modeling we need the density distribution of the hydrogen gas, the flux of solar Lyman alpha photons, and the scattering cross section. We need also a radiative transfer theory to account for the fate of photons emerging from individual H atoms. In the spectral simulation we need to know the velocity distribution instead of the density distribution of the hydrogen gas. These different parts of the modeling are described briefly in the following subsections.

4.1. Hydrogen Gas Velocity Distribution

As explained in the introduction, we will ignore the time-dependent modeling of the hydrogen gas in this work. Then the velocity distribution can be obtained in a closed form. This so-called Danby-Camm solution assumes that at infinity the velocity distribution is Maxwellian and that there are no H-H collisions. In the case of vanishing ionization the solution is [*Danby and Camm*, 1957; *Wu and Judge*, 1979, 1980; *Kyrölä et al.*, 1994]

$$W(\vec{v}, \vec{r}) = \frac{1}{(2\pi)^{3/2} v_T^3} e^{-\frac{1}{2v_T^2} f(\vec{v}, \vec{r})} \tag{2}$$

Here v_T is the thermal width ($v_T = \sqrt{kT/m}$) and

$$f(\vec{v}, \vec{r}) = v_b^2 + v_0^2 - 2v_b v_0 \frac{v_z(v_0 - v_r) - V(r)\cos\theta}{v_0(v_0 - v_r) - V(r)} \tag{3}$$

where

$$v_0 = \sqrt{v^2 + 2V(r)} \tag{4}$$

is the initial velocity of a particle now at the point $(\vec{r}, \vec{v})$ and

$$V(r) = -\frac{GM}{r}(1 - \mu) \tag{5}$$

is the potential of the central force at a distance r from the Sun. The gravitational constant is G, M is the solar mass, and μ is the ratio between the repulsive radiation pressure force from solar Lyman alpha and the attractive gravitational force. The solution is given in the coordinates where the z-axis is parallel with the incoming flow and θ is the angle between the r-vector and z-axis. The initial bulk velocity of the flow has been designated by v_b.

4.2. Ionization Modeling

The inclusion of the ionization for the loss free distribution (2) is an important part of the modeling, because we are interested in estimating the ionization parameters from data. It can be accomplished quite simply. The velocity distribution at the point $(\vec{r}, \vec{v})$ is multiplied by a factor

$$e^{-\int \beta[\vec{r}(t)]dt} \tag{6}$$

Here β is the ionization rate of the H atom at $\vec{r}$, and we are integrating from the time of observation to the past along the atom trajectory in the heliosphere. In the special case when the ionization rate is dependent only on the radial distance to the Sun this multiplicative factor can be calculated further and it is given by

$$e^{-\int \beta dt} = e^{-\frac{\beta_e r_0^2}{v_0 |p|}\Delta\phi} \tag{7}$$

where β_e is the ionization rate at r_0=1 AU, p is the impact parameter, and $\Delta\phi$ is the angle sweeped by the particle trajectory [see *Fahr et al.*, 1971; *Summanen et al.*, 1993].

The name of SWAN already brings forth the idea that the simple isotropic modeling given by (7) is not adequate. We are after possible anisotropies of the Sun. We write the solar ionization rate as

$$\begin{aligned} \beta(\theta) &= \beta_0[\Theta(\theta)(1 - A_N \sin^2\theta) \\ &+ \Theta(-\theta)(1 - A_S \sin^2\theta) + B(\theta)] \end{aligned} \tag{8}$$

Here the angle θ is the solar heliographic latitude, Θ is the step function restricting either of the first two terms to either the northern or southern hemisphere only. A_N and A_S are the traditional asymmetry parameters but now individually for both solar hemispheres. The last factor gives a possibility for a narrow ionization bulge around the solar equator. The origin of this feature goes back to the Prognoz Lyman alpha data where a small dip around ecliptic was observed [see *Bertaux et al.*, 1988a]. The studies by *Summanen et al.* [1996b] showed that ionization near the ecliptic may have a sharp increase. The name groove has been proposed by *Bertaux et al.* [1996a], where also a qualitative discussion of this phenomenon can be found. In this work we use the following modeling for the ionization bulge:

$$B(\theta; b_e, b_w) = b_e \exp(-\theta^2/b_w^2) \quad (9)$$

The parameter b_e gives the strength of the bulge, and b_w characterizes the width of the bulge.

Still a more general ionization model is given by the discrete model introduced by *Summanen et al.*, [1993]. The ionization distribution is defined by

$$\beta(\theta_n \leq \theta \leq \theta_{n+1}) = \beta_n \quad (10)$$

In this study we will, however, exploit only the analytical model (8).

4.3. Radiative Transfer

We assume that the hydrogen gas is optically thin and the Lyman alpha field can be described by a single scattering radiative transfer. The spectral modeling is then based on the following formula [*Brasken and Kyrölä*, 1996]:

$$I(\omega_{\mathbf{q}}) = \frac{8\pi\alpha^2 R^4 \omega_{\mathbf{q}}^3 \phi_0 r_0^2}{27c\Gamma} \times \int \frac{P(\theta(s))ds}{r(s)^2} \int d\mathbf{v}_\perp W\left[\Lambda_{\mathbf{q}}, \mathbf{v}_\perp, \vec{r}(s)\right] \quad (11)$$

where α is the fine structure constant, R is the radial part of the dipole matrix elements, Γ is the decay constant, and ϕ_0 is the solar Lyman alpha flux at $r = 1$ AU. In the arguments of the velocity distribution function the first one is $\Lambda_{\mathbf{q}} = c[(\omega_{\mathbf{q}} - \omega_\alpha)/\omega_{\mathbf{q}}]$, where ω_α is the Lyman alpha frequency. The velocity distribution is integrated over the velocities ($\mathbf{v}_\perp$) which are transversal to the line of sight. The scattering phase function is

$$P(\theta) = \frac{11}{12} + \frac{3}{12}\cos^2\theta \quad (12)$$

which is normalized in unity.

The photometric signal can be expressed from (11) as

$$I = \sigma\phi_0 r_0^2 \int \frac{P(\theta(s))n[\vec{r}(s)]}{r(s)^2} ds \quad (13)$$

The cross section σ is

$$\sigma = \frac{e^2 R^2}{6\hbar\epsilon_0}\left(\frac{\lambda_\alpha}{c}\right) \quad (14)$$

and the density is given by

$$n = \frac{c}{\lambda_\alpha} \int d\lambda \int d\mathbf{v}_\perp W\left[\Lambda_{\mathbf{q}}, \mathbf{v}_\perp, \vec{r}(s)\right] \quad (15)$$

The hydrogen density can also be calculated using the unperturbed velocity distribution at infinity [*Lallement et al.*, 1985a; *Summanen*, 1996b]. The numerical agreement between these two methods are better than 1%. This type of modeling of interplanetary H, which takes into account the full thermal velocity distribution of H atoms "at infinity,", is often referred in the literature as "the hot model."

5. Cases Studies

In order to analyze the possibility for a solar ionization anisotropy we need to make sure that the other parameters of the model are reasonably correct. We have selected the following parameters to establish a reference case:

For the incoming wind we assume that

$$\begin{aligned} v_b &= 20 \text{ km/s} \\ \phi_{wind} &= 254° \\ \theta_{wind} &= 7.5° \\ T &= 7500 \text{ K} \\ n_{inf} &= 0.1 \text{ cm}^{-3}. \end{aligned}$$

The first three fix the interstellar wind bulk velocity and direction. The last two fix the temperature and the density of the H cloud.

For the Sun we assume

$$\begin{aligned} \mu &= 0.75 \\ \phi_0 &= 3.3 \times 10^{11} \text{ ph/(cm}^2\text{s}\mathring{A}) \\ \beta_0 &= 4.0 \times 10^{-7} \text{ s}^{-1} \\ A_N &= A_S = 0.4 \\ b_e &= 0. \end{aligned}$$

This reference case will be our starting point in our search for the best possible parameters for our model with a strong emphasis on the solar wind parameters β_0, A_N, A_S, b_e, and b_w. Our parameter space is 12 dimensional. With the single scattering approximation the solar Lyman alpha flux and the interstellar hydrogen density cannot be resolved; that is, they form a scaling factor. This leaves still 10 parameters (plus scaling) to be analyzed. Because of the computational requirement of the forward model it is clear that a full search for optimal parameters in this problem cannot be performed even if we had a reasonable starting point in the parameter space.

Our strategy is then to use the locations denoted by UW, RW, LW, and DW in Figure 2 for a search of parameters. Instead of wandering to random points in the 10-dimensional parameter space, we first make a general assessment by restricting changes from the reference point along each parameter axes only, that is, we change only one parameter at a time. Obviously, this strategy does not constitute a sufficient parameter study, but it gives indications of the influences of each parameter. After this step we fine-tune the ionization model.

The following values will be tried in the first step

$$\begin{aligned} \mu &= 0.6, 0.75, 0.9, 1.2 \\ T &= 6000, 7500, 9000 \text{ K} \\ v_b &= 15, 20, 25 \text{ km/s} \\ \theta_{wind} &= 0°, 7.5°, 15° \\ \phi_{wind} &= 250°, 254°, 258° \end{aligned}$$

$$\begin{aligned} \beta_0 &= 2.0, 4.0, 8.0 \cdot 10^{-7}\ \mathrm{s}^{-1} \\ A_N &= 0, 0.4 \\ A_S &= 0, 0.4 \\ b_e &= 0.0, 1.0. \end{aligned}$$

The width of the bulge is kept constant at $b_w = 11.5°$.

We also present results for the isotropic reference model; that is, we use the reference parameters but set the ionization model isotropic ($A_N = A_S = b_e = 0$).

In all simulations we will use the actual SOHO location and velocity to build up the simulation. The simulation scan plane is equal to the one used to pick up the data. Data are pixel counts on which flat-field correction has been applied. The absolute calibration will not be considered, but the different sensitivities of plus and minus sensors will be taken into account.

The first test place is the upwind location (UW). Using the reference value 254° for the interstellar wind longitude the correct date for the SOHO UW location would be June 3, 1996. Because of data availability we have selected a day earlier, June 2, 1996. Figure 5a shows SWAN data and the reference model with all the modifications listed above. We have not cared about the absolute calibration, but we have brought artificially all the curves to meet at the center of Figure 5a. In this way we can better see how the parameters affect the two hemispheres. It is quite obvious that all parameters except the bulge strength (b_e) are rather noninfluental if we try to reach an agreement between data and the model. Some improvements are achieved if we increase the ionization rate, decrease the bulk velocity, or decrease the longitude of the interstellar wind direction.

Because the large intensity decrease (groove) around the ecliptic deviates so much from the models we try to look at data and models differently. In Fig. 5b we bring all the curves to meet at the north ecliptic pole. Now we can see that the isotropic model which looked totally inadmissible in Figure 5a does not look so drastically impossible any more. It gives about the right amplitude near the poles but the ecliptic region is still not right. Notice that even the isotropic model delivers unequal intensities to different hemispheres. The explanation is that the interstellar wind is not traveling exactly in the ecliptic but in a few degrees angle with respect to it. Again, the increase in the overall ionization rate gives a better agreement, but the declines from polar regions seem too rapid. The reference case with a bulge looks already quite right near the ecliptic, but the pole directions show that the harmonic anisotropy is too large. Reducing the degree of the harmonic anisotropy we finally reach quite a satisfactory fit with the data (black triangles). The best fit parameters differing from the reference case are $b_e = 0.9$, $A_N = 0$, and $A_S = 0.05$.

We now move to the right wind position (RW). The data set is achieved on September 1, 1996 (4° off from the correct RW position). Figure 6 shows, again, the data and the different models which are all brought together at the center. Stars in the southern hemisphere now make data fitting a more suspicious job. The differences between the models and the data are now moderate compared to the upwind location. Improvements are brought by an increase in the ionization rate, a decrease in the harmonic anisotropy, and an increase of the bulk velocity or the radiation pressure. A reasonable fit can be achieved by starting from a nearly isotropic case

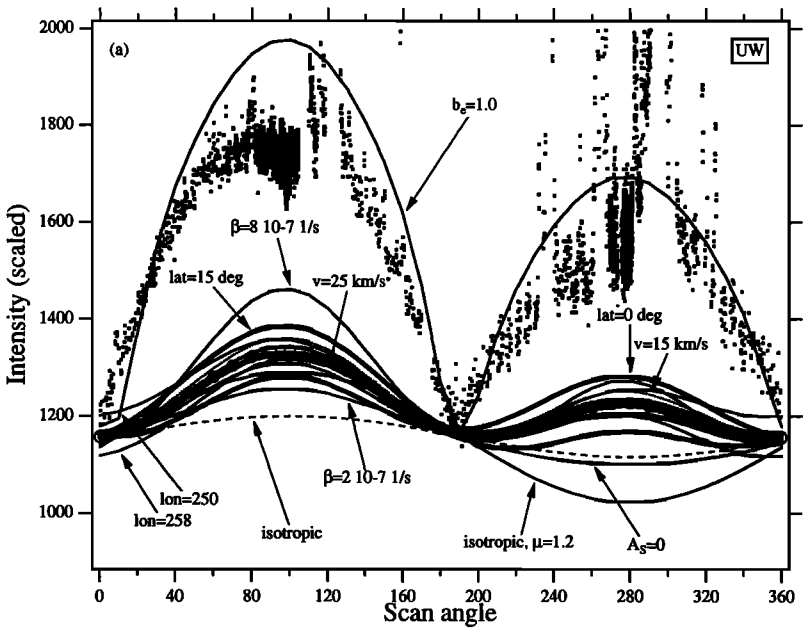

Figure 5a. Upwind modeling. The curves are brought to meet in the center. The reference case is shown by open circles and the isotropic case by the dashed line. The heavier lines show results when the wind latitude angle has been varied, $\theta_{wind} = 0, 15°$.

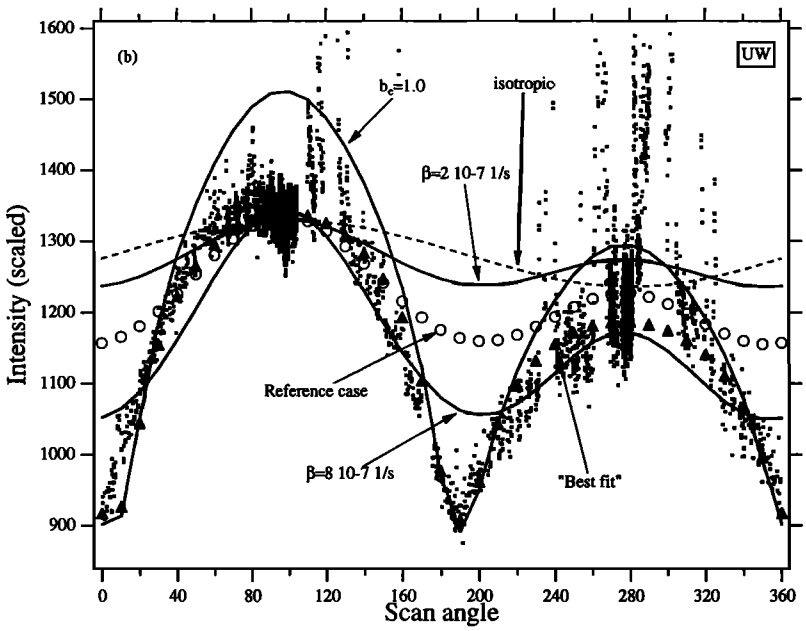

Figure 5b. Same as Figure 5a, except that only a few curves are shown, and they are brought to meet at the north ecliptic pole (except the bulge case). The best fit is shown by black triangles.

with the bulge. The bulge is now smaller than in the upwind case. The best fit parameters differing from the reference case are $b_e = 0.4$, $A_N = 0.1$, and $A_S = 0.2$.

The left wind (LW) data are from March 5, 1996 (2° off from the correct position). The overall photometric pattern should be the same as in the right wind position but shifted by 180°. In Figure 7 we have shown only a few model calculations. Both the isotropic case and the reference cases deviate from the data in a significant way. The case with $\mu = 0.9$ which showed a good agreement with data in the RW case fails. A model with a bulge gives again a reasonable fit. The best fit parameters differing from the reference case are $b_e = 0.25$, $A_N = 0.05$, and $A_S = -0.1$.

The downwind location (DW) data are from December 1, 1996 (2° from the correct downwind position). The first thing to note in Figure 8 is that data display several stars which seriously harm the identification of the diffuse background in the southern hemisphere. The agreement between the models and the data in the southern hemisphere is poor. These data seem difficult for any parameter tuning effort, and we back up to

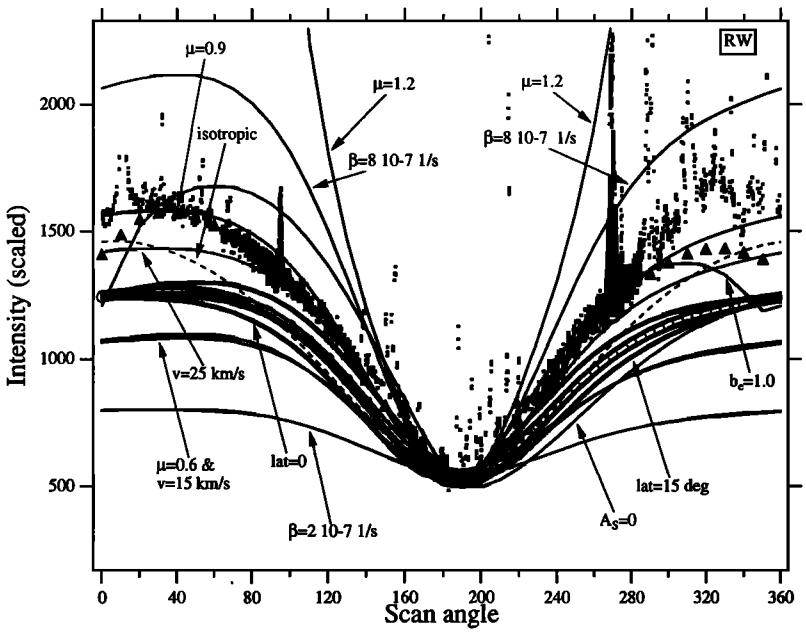

Figure 6. Right wind modeling. The best fit shown by black triangles.

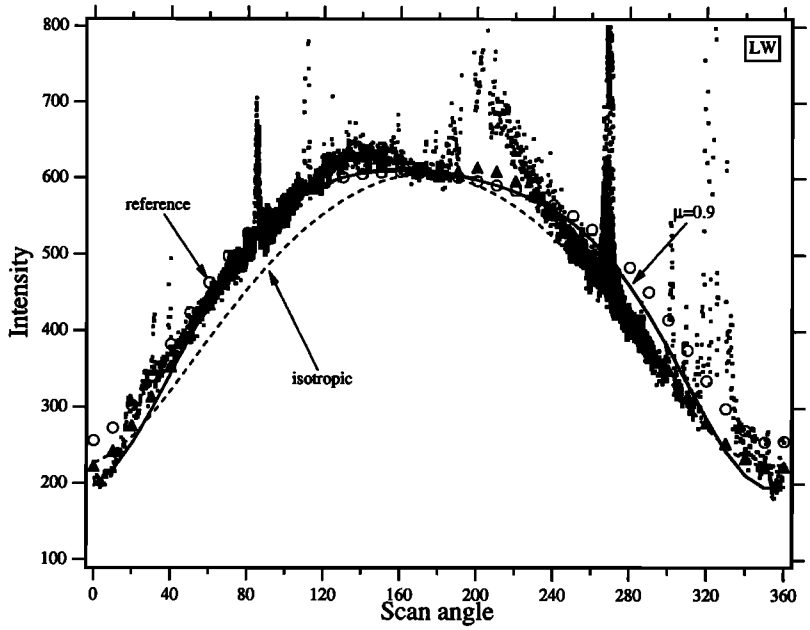

Figure 7. Left wind modeling. The best fit is shown by black triangles.

data 2 weeks earlier on November 13, 1996. This location is the same as in the Prognoz measurement session S3, and we have drawn both data in Figure 9. We show that the reference case and the isotropic model differ from data by significant amounts but the bulge model fits data reasonably well. The best fit parameters differing from the reference case are now $b_e = 0.4$, $A_N = 0.1$, and $A_S = 0.1$.

6. Solar Wind Mass Flux

In section 5 we obtained total ionization rates (i.e., parameters A_N, A_S, b_e, and b_w) as a function of solar heliographic latitude for several measurement positions. The rates are shown together in Figure 10. The parameters for the ionization model are listed in Table 1. The rates are almost flat except inside a narrow latitude belt

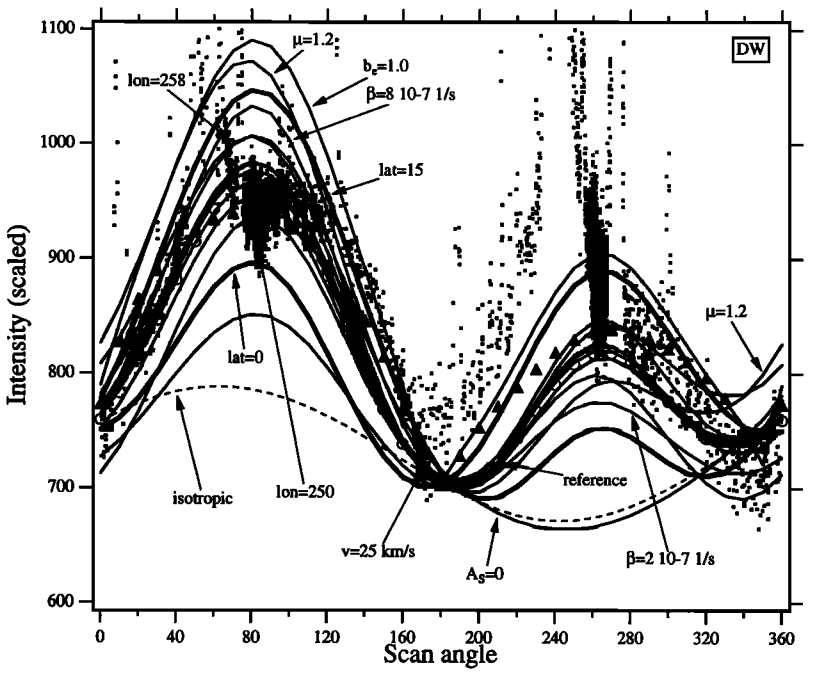

Figure 8. Downwind modeling. No reasonable fitting was achieved in this case. The best fit is shown by black triangles.

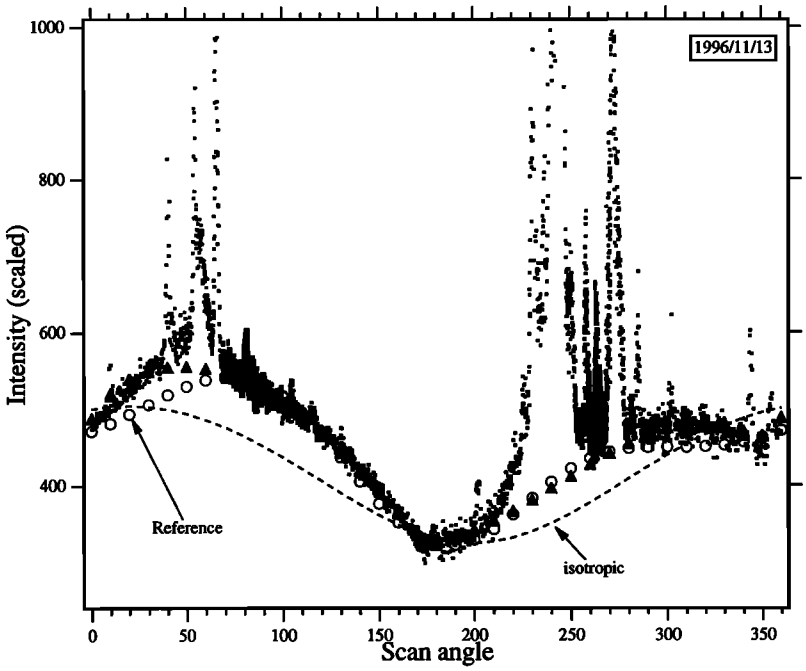

Figure 9. SWAN data on November 13, 1996, with the reference model (circles), the isotropic model (dashed curves), and the best fit model (black triangles). The location is the same as in the Prognoz session S3.

from -20° to 20°. All cases show an ionization bulge inside this region.

From the ionization rate we can estimate the solar wind mass flux by the formula

$$\beta(\theta) = \beta_{ph} + n(\theta) v_{SW}(\theta) \sigma[v(\theta)] \qquad (16)$$

We assume that the photoionization rate β_{ph} is 20% of the total ionization rate and it is independent on latitude. We use the known charge exchange cross section and assume the solar wind velocity distribution to follow the Ulysses measurements [*Goldstein et al.*, 1996]. The ensuing solar wind mass flux is shown in Figure 11.

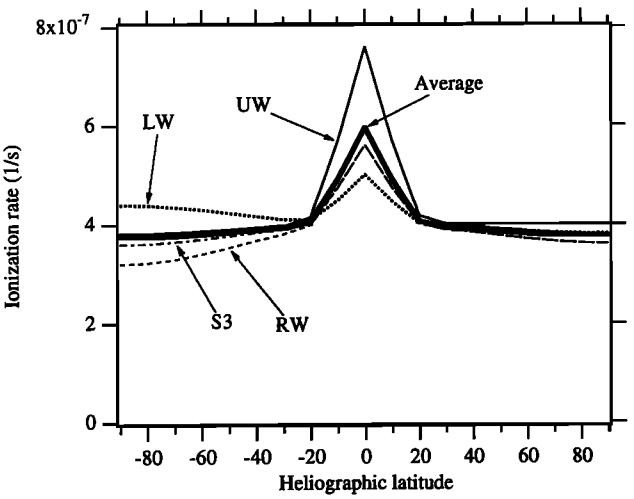

Figure 10. All ionization models. The average ionization model is also shown (thicker line).

The mass flux is flat outside the central region where it shows a clear bulge. The reduction of the mass flux from the equator to the poles is in the UW case 35% and in average 18%.

7. Conclusions

In this work we have done the first analysis of the solar wind mass flux distribution based on SWAN Lyman alpha data. The solar wind anisotropy is the principal scientific objective of the SWAN mission. We have used SWAN data in a limited selection. The samples we have analyzed try to mimic the Prognoz-satellite measurements in 1976-1977 as Prognoz measurements have been the main source for the solar wind anisotropy studies earlier. The appearance of stars in our data sets have made the comparison between models and data difficult. Removing the stars by inspection was attempted but large data gaps ensued and this approach was not continued.

Despite the difficulties with data quality we have confirmed to some degree of confidence the earlier results obtained from the analysis of the Prognoz data. The solar wind looks isotropic for all latitudes except the narrow belt around the solar equator.

Table 1. Ionization Parameters for SWAN Data

Data	A_N	A_S	b_e
LW	0.05	-0.1	0.25
UW	0.0	0.05	0.9
RW	0.1	0.2	0.4
S3	0.1	0.1	0.4

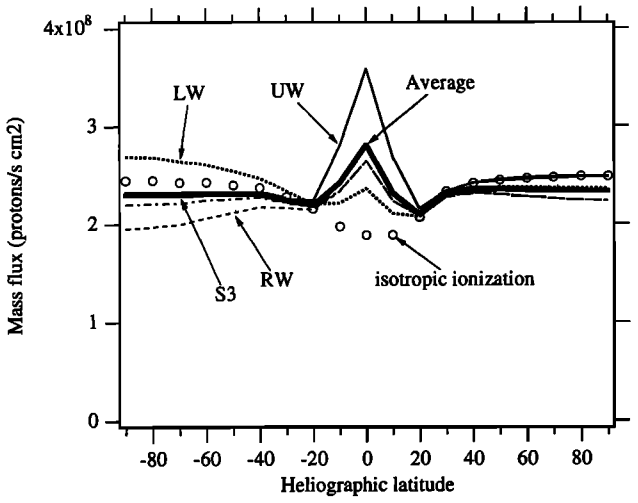

Figure 11. Results for the solar wind mass flux. The average mass flux is also shown (thicker line). Mass flux from an isotropic ionization is shown by circles. The latitudinal variation in this case is caused by the velocity dependence of the charge exchange cross section.

It is quite obvious that in future studies of the solar wind distribution we must try to avoid data contamination by stars. This can be accomplished by searching star void regions and performing the data fitting using preselected directions into void directions. Both photometric and spectral data must be considered for parameter analysis. This will restrict the feasible parameter space which in this work was impractically large. The use of data from other sources must also be considered for this same purpose. Finally, the model itself must be completed to include absorption and multiple scattering, solar cycle effects, the influence of the heliospheric interface, and probably the possibility for an anisotropy of the solar UV field. After these steps we can perform a more assuring but also much more demanding data analysis.

Acknowledgments. The Editor thanks H. Fahr and V. G. Kurt for their assistance in evaluating this paper.

References

Ajello, J.M., Solar minimum Lyman alpha sky background observations from Pioneer Venus orbiter ultraviolet spectrometer: solar wind latitude variation, *J. Geophys. Res., 95*, 14855, 1990.

Baranov, V. B. and Y. G. Malama, Model of the solar wind interaction with the local interstellar medium: numerical solution of self-consistent problem, *J. Geophys. Res. 98*, 15157, 1993.

Bertaux, J. L., and R. Lallement, Analysis of interplanetary Lyman-alpha line profile with a hydrogen absorption cell: theory of the Doppler angular spectral scanning method, *Astron. Astrophys., 140*, 230, 1984.

Bertaux, J. L., R. Lallement, V. G. Kurt, and E.N. Mironova, Characteristics of the local interstellar hydrogen determined from Prognoz 5 and 6 interplanetary Lyman alpha line profile measurements with a hydrogen absorption cell, *Astron. Astrophys., 150*, 1, 1985.

Bertaux, J. L., et al., *SWAN, A Study of Solar Wind Anisotropies, Proposal for the ESA SOHO-mission (1987)*, European Space Agency, Paris, 1988a.

Bertaux, J.L., et al., SWAN: A study of solar wind anisotropies, in The SOHO Misssion, *European Space Agency Spec. Publ., SP-1104*, 1988b.

Bertaux, J. L., et al., SWAN: A study of solar wind anisotropies on SOHO with Lyman alpha sky mapping, *Sol. Phys., 162*, 403, 1995.

Bertaux, J.L., E. Quemerais, and R. Lallement, Observations of a sky Lyman alpha groove related to enhanced solar wind mass flux in the neutral sheet, *Geophys. Res. Lett., 23*, 3675, 1996a.

Bertaux, J. L., R. Lallement, and E. Quemerais, UV studies and the solar wind, *Space Sci. Rev., 78*, 317, 1996b.

Bertaux, J.L, E. Quemerais, R. Lallement, E, Kyrölä, and T. Summanen, Comments on the paper: Recalculation of H-Ly alpha sky surveys: No need for anisotropic solar wind mass outflows?, *Sol. Phys., 170*, 365, 1997a.

Bertaux, J.L., E. Quemerais, R. Lallement, E. Kyrölä, W. Schmidt, T. Summanen, M. Berthe, J-P. Goutail, and J. Costa, First results from SWAN Lyman alpha solar wind mapper on SOHO, *Sol. Phys., 175*, 737, 1997b.

Bertaux, J.L, J. Costa, E. Quemerais, R. Lallement, E. Kyrölä, W. Schmidt, T. Summanen, T. Mäkinen, and C. Goukenlauque, Lyman-alpha observations of comet Hyakutake with SWAN on SOHO, *Planet. Space Sci.*, in press, 1997c.

Brasken, M., and E. Kyrölä, Resonance scattering of Lyman alpha from neutral hydrogen, *Astron. Astrophys.*, in press, 1997.

Danby, J.M.A., and G.L. Camm, Statistical dynamics and accretion, *Monthly Notices Roy. Astron. Soc., 117*, 50, 1957.

Fahr, H., The interplanetary hydrogen cone and its solar cycle variations *Astron. Astrophys., 14*, 1971.

Fahr, H., The interstellar gas flow through the heliospheric interface region, *Space Sci. Rev., 78*, 199, 1996.

Goldstein, B. E., M. Neugebauer, J. L. Phillips, S. Bame, J. T. Gosling, D. McComas, Y.-M. Wang, N. R. Sheeley, and S. T. Suess, Ulysses plasma parameters: Latitudinal, radial, and temporal variations, *Astron. Astrophys., 316*, 296, 1996.

Holzer, T. E., Neutral hydrogen in interplanetary space, *Rev. Geophys., 15*, 467, 1977.

Keller, H.U., K. Richter, and G. E. Thomas, Multiple scattering of solar resonance radiation in the nearby interstellar medium II, *Astron. Astrophys., 102*, 415, 1981.

Kumar, S. and A. L. Broadfoot, Evidence from Mariner 10 of solar wind flux depletion at high ecliptic latitudes, *Astron. Astrophys., 69*, L5, 1978.

Kumar, S. and A. L. Broadfoot, Signatures of solar wind latitudinal structure in interplanetary Lyman-α emissions: Mariner 10 observations, *Astrophys. J., 228*, 302, 1979.

Kyrölä, E., T. Summanen, and P. Räback , Solar cycle and interplanetary hydrogen, *Astron. Astrophys., 288*, 299, 1994.

Lallement, R., Relations between ISM inside and outside the heliosphere, *Space Sci. Rev., 78*, 361, 1996a.

Lallement, R., J. L. Bertaux, V. G. Kurt, and E.N. Mironova, Observed perturbations of the velocity distribution of interstellar hydrogen atoms in the solar system with Prognoz Lyman-alpha measurements, *Astron. Astrophys., 140*, 243, 1984.

Lallement, R., J. L. Bertaux, and F. Dalaudier, Interplanetary Lyman a spectral profiles and intensities for both repulsive and attractive solar force fields: predicted absorption pattern by a hydrogen cell, *Astron. Astrophys., 150*, 21, 1985a.

Lallement, R., J. L. Bertaux, and V. G. Kurt, Solar wind decrease at high heliographic latitudes detected from Prognoz interplanetary Lyman alpha mapping, *J. Geophys. Res.*, *90*, 1413, 1985b.

Lallement, R., T. E. Holzer, and R. H. Munro, Solar wind expansion in a polar coronal hole: inferences from coronal white light and interplanetary Lyman alpha observations, *J. Geophys. Res.*, *91*, 6751, 1986.

Lallement, R., and P. Bertin, Northern-hemisphere observations of nearby interstellar gas: possible detection of the local cloud, *Astron. Astrophys.*, *266*, 479, 1992.

Lallement, R., E. Kyrölä, and T. Summanen, Interstellar gas in the heliosphere, *Space Sci. Rev.*, *72*, 455, 1995.

Osterbart, R and H. J. Fahr, A boltzman-kinetic approach to describe the entrance of neutral interstellar hydrogen into the heliosphere *Astron. Astrophys.*, *264*, 260, 1992.

Pryor, W. R. et al., Latitude variations in interplanetary Lyman alpha dat from Galileo EUVS modeled with solar He 1083 nm images, *Geophys. Res. Lett.*, *23*, 1893, 1996.

Quemerais, E., and J.L. Bertaux, Radiative transfer in the interplanetary medium at Lyman alpha, *Astron. Astrophys.*, *277*, 283, 1993a.

Quemerais, E., R. Lallement, and J-L. Bertaux, Lyman alpha observations as a possible means for the detection of the heliospheric interface, *J. Geophys. Res.*, *98*, 15199, 1993b.

Ripken, H. W. and H.J. Fahr, Modification of the local interstellar gas properties in the heliospheric interface, *Astron. Astrophys.*, *122*, 181, 1983.

Rucinski, D. and M. Bzowski, Modulation of interplanetary hydrogen density distribution during the solar cycle, *Astron. Astrophys.*, *296*, 248, 1995.

Scherer, H., and H. J. Fahr, Recalculation of H-Lα sky surveys: no need for anisotropic solar wind mass outflows?, *Solar Phys.*, *161*, 383, 1995.

Scherer, H., and H. J. Fahr, H Lyman alpha transport in the heliosphere based on an expansion into scattering hierarchies, *Astron. Astrophys.*, *309*, 957, 1996.

Scherer, H., and H. J. Fahr, Reply to the reply: New need for latitudinal asymmetries, *Solar Phys.*, *170*, 371, 1997.

Summanen, T., The effect of the time and latitude dependent solar ionization rate on the measured Lyman alpha intensity, *Astron. Astrophys.*, *314*, 663, 1996a.

Summanen, T., Interplanetary Lyman alpha measurements as a tool to study solar wind properties, Ph.D. thesis, University of Helsinki, Helsinki, Finland, 1996b.

Summanen, T., R. Lallement, J.L. Bertaux, and E. Kyrölä, Latitudinal distribution of solar wind as deduced from Lyman alpha measurements: An improved method, *J. Geophys. Res.*, *98*, 13215, 1993.

Summanen, T., R. Lallement, J.L. Bertaux, and E. Kyrölä, Correction to latitudinal distribution of solar wind as deduced from Lyman alpha measurements: an improved method, *J. Geophys. Res.*, *99*, 19375, 1994. **(Correction,** *J. Geophys. Res.*, 98, 13215, **1993.)**

Summanen, T., R. Lallement, and E. Quemerais, Solar wind proton flux latitudinal variations: Comparisons between Ulysses in situ data and indirect measurements from interstellar Lyman alpha mapping, *J. Geophys. Res.*, *102*, 7051, 1997.

Wu, F. M., and D. L. Judge, Temperature and flow of the interplanetary gases along solar radii, *Astrophys. J.*, *231*, 594, 1979.

Wu, F. M., and D. L. Judge, A reanalysis of the observed interplanetary hydrogen La emission profiles and the derived local interstellar gas temperature and velocity, *Astrophys. J.*, *239*, 389, 1980.

J.-L. Bertaux, J. Costa, R. Lallement, and E. Quemerais, Service d'Aeronomie du Centre National de la Recherche Scientifique, BP 3, 91370 Verrieres le Buisson, France.

E. Kyrölä, T. Mäkinen, W. Schmidt, and T. Summanen, Geophysical Research Division, Finnish Meteorological Institute, FIN-00101, Helsinki, Finland. (e-mail: erkki.kyrola@fmi.fi)

(Received July 7, 1997; revised November 4, 1997; accepted November 20, 1997.)